The 6th ASME-JSME Thermal Engineering Joint Conference
March 16-20, 2003

TED-AJ03-420

IMPACT OF SKIN EFFECT ON THERMAL BEHAVIOR OF RF MEMS SWITCHES

Brian D. Jensen
Department of Mechanical Engineering
University of Michigan
Ann Arbor, Michigan 48109
bdjensen@umich.edu

Kazuhiro Saitou
Department of Mechanical Engineering
University of Michigan
Ann Arbor, Michigan 48109
kazu@umich.edu

John L. Volakis
Electrical Engineering and Computer Science
University of Michigan
Ann Arbor, Michigan 48109
volakis@umich.edu

Katsuo Kurabayashi
Department of Mechanical Engineering
University of Michigan
Ann Arbor, Michigan 48109
katsuo@umich.edu

Keywords: reliability of RF MEMS switches, skin effect, current modeling

ABSTRACT

Future high-performance communications systems require increasing functionality and performance reliability at smaller size and power consumption. Microelectromechanical Systems (MEMS) have been identified as a promising enabling technology with the potential for a major impact on existing RF architectures by reducing weight, cost and size, and power dissipation. In particular, RF MEMS switches show many technological advantages over conventional switches based on a p-n diode, especially reduced power consumption.

Despite this technological promise, the reliability of RF MEMS is critical to commercialize the technology for practical telecommunications applications. When the MEMS structure is operated under high RF power, heat is locally produced and selectively distributed due to metal and dielectric losses. This problem is particularly serious at frequencies above approximately 2 GHz, where electron crowding becomes significant at the edge of the signal transmission metal strip of the RF MEMS switch. Localized heating due to this "skin effect" can cause switch failure. This manuscript considers the impact of the skin effect on the local temperature distribution and thermal reliability of RF MEMS switches.

Prediction of temperature rise due to electrical losses requires multi-domain modeling. The current distribution in the switch is modeled using a 2-D finite element-boundary integral model of beam cross-sections. Average power dissipation in the switch is determined using the results of the electromagnetic model. The temperature in the switch is then calculated using a 2-D heat transfer finite element model. Because the current distribution depend on temperature, the electromagnetic and thermal models iterate on the current and temperature solutions until convergence is achieved. This represents the first time thermal and high-frequency electromagnetic simulations have been linked in multi-domain solutions.

The model is used to predict the dominant failure mechanism in a gold beam 400 μm long, 50 μm wide, and 2 μm thick. Two candidate mechanisms are studied: creep and buckling. Using the temperature modeling, the onset of these failure mechanisms is predicted in Fig. A-1 as a function of both frequency and RF power input. The modeling shows that failure is more likely to occur as either frequency or power increases. Frequency rise has not previously been linked to temperature increase because previous modeling efforts have not included the skin effect. Thus, for this beam geometry, buckling due to thermal stress is found to dominate, with a temperature rise of only 10°C before buckling occurs.

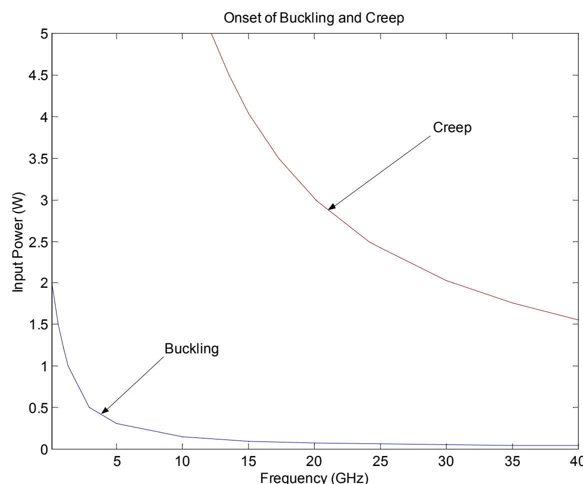

Figure A-1: Predicted onset of buckling and creep

Copyright © 2003 JSME

INTRODUCTION

Emerging and future needs for autonomous, wireless communications systems require high-quality, highly reliable electronic components with very low power consumption. Micromechanical switches present a promising technology to meet this demand. Such switches carrying radio frequency (RF) signals have been demonstrated with low loss, low distortion of the electrical signal, greater power-carrying capability, and high off-state isolation compared to semiconductor switches, such as *p-n* diodes or field effect transistors [1-3]. They also consume negligible power, which makes them especially attractive for battery-operated, autonomous communication systems [4,5]. Drawbacks of mechanical switches include slow switching speeds (approximately 10 µs, compared to nanoseconds or faster for semiconductor switches) and high actuation voltage (~5-50 V) [6].

However, a major drawback of micromechanical switches is their reliability [7]. Before such switches can be used in many commercial applications, they must demonstrate the ability to switch reliably over billions of cycles. Moreover, their power handling capability is normally much lower than 1 W, and reliability concerns become more pronounced for higher power [8]. To design more reliable switches with better power handling capability, careful modeling of the switches is required.

One of the most important factors in determining the reliability of RF micromechanical (RF MEMS) switches is their thermal capabilities. A previous paper on thermal modeling of RF MEMS switches concludes that thermal effects may be insignificant for one switch design [9]; however, our work indicates that thermal effects can be very important for another class of switch designs. Many of the possible failure mechanisms for MEMS switches, such as electromigration, creep, adhesion, buckling, and surface degradation, are related to the switch temperature. Even small electrical losses can cause significant temperature rise for MEMS components, making thermal modeling essential to understand and predict failure. The electron crowding caused by the skin effect at high signal frequency tends to make this problem worse. Hence, careful modeling of both electrical and thermal effects is needed to yield a better understanding of switch failure. This model can then be used in optimal switch design.

Developing such a model is difficult because it must predict multi-domain behavior. The model must account for both electromagnetic and thermal effects. Previous work in multi-domain modeling includes development of models relating electrostatic force to mechanical deformation [10,11] and modeling of temperature rise due to DC current flow [12]. This paper presents fundamental work in developing a method to link high-frequency electromagnetic and thermal modeling. Numerical models are presented for both electrical and thermal phenomena, and integrated modeling provides multi-domain solutions. Sample model data is presented to demonstrate trends, and evaluation of some failure modes is demonstrated.

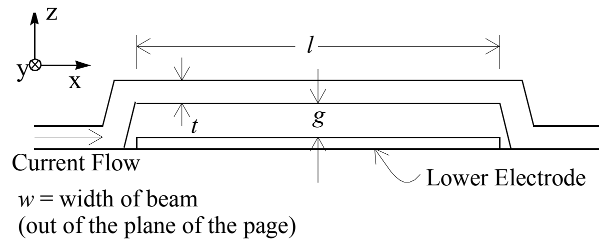

Figure 1: Longitudinal cross-section of a RF MEMS switch

MODELING OVERVIEW

Figure 1 shows a longitudinal cross section of a typical RF MEMS switch which is normally on. The switch consists of a current-carrying beam. To turn off the switch, electrostatic force applied from the lower electrode could pull the beam down until it contacted the lower electrode, providing an alternate current path. Typical dimensions for such a beam are length (l) from 100-1000 µm, width (w) from 20-200 µm, thickness (t) from 0.5-10 µm, and gap (g) from 0.1-3.0 µm. The beam and lower electrode are usually metal, often gold because of its high electrical conductivity. Such switches typically operate at a signal frequency between 100 MHz and 100 GHz.

Current Modeling

For this initial work, the beam will be modeled only in the up state shown in Fig. 1. This simplifies modeling by avoiding calculation of electrical and thermal contact resistance. With the current flowing through the beam, the heat generation in the beam is equivalent to the electrical power loss, which is given by

$$p_{loss} = \|J\|^2\rho \tag{1}$$

where p_{loss} is the power loss per unit volume, J is the current density, and ρ is the electrical resistivity. Hence, to calculate the heat generation in the beam, the distribution of current density throughout the beam must be known.

At low frequencies, current is spread nearly evenly though the beam, and current density can be assumed constant. However, at high frequencies, self-inductance of the conductor causes electrons to crowd toward the outside edges of the beam, a phenomenon commonly known as the skin effect. As a result, the majority of the current is carried in the outside layer, whereas the beam interior carries almost no current, reducing the effective cross-sectional area of the conductor. The effective resistance of the conductor increases as its effective area decreases, which induces a corresponding increase in the heat dissipated in the beam. For more detail on the skin effect, see a text in RF circuits, such as [13].

Because J varies harmonically with time, the power dissipation will also vary harmonically. However, for the frequencies considered in this paper (> 40 MHz), the time constant for thermal response will be much longer than the period of variation. Hence, the power dissipation can be treated constant, with its magnitude being equal to the

Copyright © 2003 JSME

average power dissipation. This paper will concentrate on finding steady-state heat transfer conditions assuming average power dissipation.

Note that, for a given level of power, the total rms current flowing in the beam is approximately equal to

$$I_{rms} = \sqrt{\frac{P_{in}}{Z_0}} \tag{2}$$

where P_{in} is the input power and Z_0 is the load impedance, assumed to be 50 Ω. However, the local current density J must be found using complex modeling. While analytical solutions exist for conductors with a circular cross-section, numerical modeling is required to accurately determine current density within a rectangular conductor.

Thermal Modeling

Once the current density is known, Eq. (1) is used to find the heat generation throughout the beam. The temperature throughout the beam must then satisfy the steady-state heat equation

$$\nabla(\kappa\nabla T) = -p_{loss} \tag{3}$$

where κ is the thermal conductivity and T is the temperature. Because the heat generation term is generated numerically, Eq. (3) is most easily solved with numerical techniques as well.

Equations (1) and (3) describe the dependence of temperature on electrical properties of the beam. Similarly, the electrical resistivity of most metals is related to their temperature via the Wiedemann-Franz law, which gives (see, for example, [14], pp. 151-152)

$$\rho = \frac{LT}{\kappa} \tag{4}$$

$L = 2.45 \times 10^{-8}$ W-Ω/K^2 is the Lorenz number. Equation (4) is valid for temperatures well above absolute zero. For several hundred degrees above room temperature, the thermal conductivity of most metals is fairly constant. Hence, the electrical resistivity is expected to vary linearly with temperature, as has been demonstrated experimentally [15]. This produces a positive feedback effect, as higher temperatures increase the electrical resistivity, which further increases the heat generation, as given by Eq. (1). Note also that the current density distribution will change with resistivity.

Integrated Modeling

Figure 2 shows a flow chart for a multi-domain modeling scheme which uses the relaxation method of iteration. The modeling begins with the beam at room temperature. After calculating current density using the electromagnetic model, heat generation in the beam is determined. The thermal model then solves for beam temperature. If the change in beam temperature from the preceding iteration is small, the algorithm stops. If temperature has not converged, the electrical resistivity is

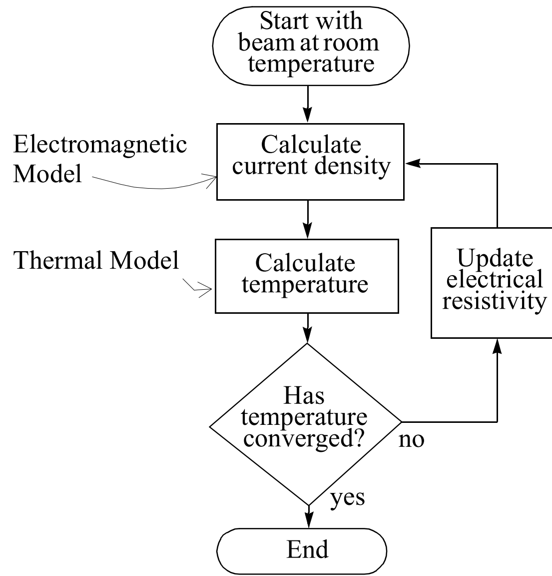

Figure 2: Flowchart for modeling temperature rise in the switch

recalculated throughout the beam using Eq. (4), and the process starts again. While this iteration scheme is quite simple, it yields satisfactory results. If required, a more complex scheme, such as Newton's method, can be implemented later.

Failure Mechanisms

As already mentioned, possible failure mechanisms in the switch include buckling, creep, adhesion, surface degradation, and electromigration. In this initial work, only buckling and creep will be considered.

Creep Failure- Creep is the time-dependent plastic deformation of materials even when they are subjected to stress well below the yield strength. Many materials, including metals, experience pronounced creep at temperatures above half the melting point of the material (see [16], pp. 215-217). While creep will occur below this point, it gives a reference temperature for consideration of creep as a failure mechanism. Hence, a gold switch, with melting point of 1340 K, is considered likely to fail over time if the temperature exceeds 670 K, or 392°C.

Buckling Failure- Buckling due to thermal stress is predicted by the Euler buckling formula

$$P_{cr} = \frac{C\pi^2 EI}{(l)^2} \tag{5}$$

where P_{cr} is the critical buckling load on the beam, E is Young's modulus, I is the first moment of inertia, and C is a constant which depends on the end conditions of the beam. For an ideal fixed-fixed beam, C is 4. This equation implicitly assumes that Young's modulus is constant throughout the beam. Because of temperature gradients in the beam, this assumption may not be completely accurate, but variations in Young's modulus are not expected to exceed a few percent over the temperature range of interest. Hence, for a gold beam (E = 80 GPa) of length

Copyright © 2003 JSME

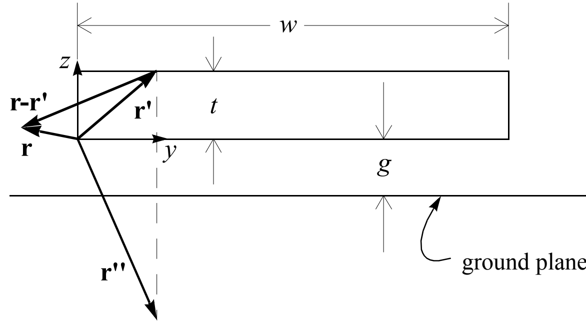

Figure 3: Beam cross-section used in electromagnetic modeling

400 μm, with width of 50 μm and thickness of 2 μm, the critical buckling load is expected to be about 658 μN, which corresponds to an average strain of $8.22\text{x}10^{-5}$.

Ignoring residual strain, the beam load depends on the thermal strain in the beam. For a fixed-fixed beam, the average compressive thermal strain ε_{th} is given by

$$\varepsilon_{th} = \frac{1}{l}\int_0^l \alpha \Delta T dx \tag{6}$$

where α is the thermal expansion coefficient ($13.8\text{x}10^{-6}$ per °C for gold), and ΔT is the change in temperature. The load due to thermal strain is simply the product of the thermal strain, Young's modulus, and the cross-sectional area.

ELECTROMAGNETIC MODELING

The first task in developing the integrated model is to calculate the current distribution at each point in the beam. A full-wave, three-dimensional numerical simulation is likely to give the most accurate results. However, two assumptions enhance the simplicity of the model:

- Assume that the electric field in the beam remains substantially parallel to the beam's length (the x-direction in Fig. 1), so that any y- or z- components of the current can be ignored.
- Assume that the field changes little in the x-direction, so that it may be modeled only in the y-z plane.

These assumptions allow current modeling on a transverse beam cross-section, like that illustrated in Fig. 3.

Within the beam, the electric field in the x-direction must satisfy the wave equation

$$\nabla^2 E_x - \gamma^2 E_x = 0 \tag{7}$$

which is derived from Maxwell's equations. In this equation, γ is equal to $(1+j)/\delta$. Here, j is $\sqrt{-1}$, and δ is the skin depth given by

$$\delta = \sqrt{\frac{\rho}{\pi f \mu}} \tag{8}$$

In this equation, ρ is the electrical resistivity, f is the signal frequency, and μ is the material permeability.

Using Galerkin's weighted residual method, Eq. (7) can be discretized into an equation of the form

$$\{A\}[E] + \{B\}[\psi] = [E_s] \tag{9}$$

where $[E]$ is a vector of the unknown electric field at discrete nodes in the beam and $[\psi]$ is a vector of unknown derivatives of the electric field on the boundary of the cross-section [17]. $[E_s]$ is a vector representing the source terms. Unfortunately, the field derivatives at the boundary, $[\psi]$, are unknown. Another matrix equation is required to provide enough information to solve for both $[E]$ and $[\psi]$.

The required equation can be derived using Kirchhoff's integral equation,

$$E_x(\mathbf{r}) = -\oint \left\{ G(\mathbf{r},\mathbf{r}')\frac{\partial}{\partial n'}(E_x(\mathbf{r}')) - E_x(\mathbf{r}')\frac{\partial}{\partial n'}G(\mathbf{r},\mathbf{r}') \right\} dl' \tag{10}$$

where $\frac{\partial}{\partial n'}$ represents the derivative with respect to the outward normal to the beam. The vector $\mathbf{r}$ locates the "testing point," which must be located outside of the beam or on its boundary. The vector $\mathbf{r}'$ locates the integration point. Figure 3 illustrates sample $\mathbf{r}$ and $\mathbf{r}'$ vectors. $G(\mathbf{r},\mathbf{r}')$ is the Green's function representing the field at $\mathbf{r}$ due to a point source at $\mathbf{r}'$. By careful selection of the Green's function, the solution can include the effects of the ground plane below the beam. Using electromagnetic image theory, the proper Green's function is found to be

$$\begin{aligned} G(\mathbf{r},\mathbf{r}') &= -\frac{j}{4}[H_0^{(2)}(k_0 R) - H_0^{(2)}(k_0 R'')] \\ R &= |\mathbf{r}-\mathbf{r}'| \\ R'' &= |\mathbf{r}-\mathbf{r}''| \end{aligned} \tag{11}$$

where $\mathbf{r}''$ represents the point which is a mirror image of the point $\mathbf{r}'$ reflected across the line of the ground plane, as illustrated in Fig. 3. $H_0^{(2)}(x)$ is the Hankel function of the second kind of order zero.

Equation (10) may be discretized using the boundary integral technique [18]. Specifically, using the collocation method, a set of equations can be written in matrix form as

$$\{C\}[E] + \{D\}[\psi] = [E_s'] \tag{12}$$

where $[E_s']$ represents a second source vector for the boundary integral equations. Equations (9) and (12) can be combined and solved together as

$$\begin{Bmatrix} A \\ C \end{Bmatrix}[E] + \begin{Bmatrix} B \\ D \end{Bmatrix}[\psi] = \begin{Bmatrix} E_s \\ E_s' \end{Bmatrix} \tag{13}$$

Equation (13) represents a set of equations formulated using the finite element-boundary integral technique, in

Copyright © 2003 JSME

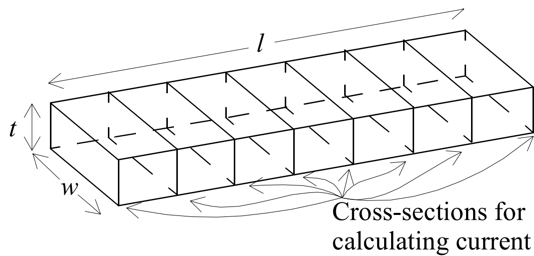

Figure 5: Micromachined beam showing several cross-sections along its length for calculating current density

which the finite element method is used to solve for interior nodes, and the boundary integral method is used to truncate the finite element mesh accurately.

The source terms in Eq. (13) must be carefully chosen to represent actual behavior in the full 3-D beam. Because the modeling is only carried out in two dimensions, adding current sources to the domain makes little sense. Instead, physical knowledge of the form of the solution is used to generate a reasonable source term. With the ground plane nearby, we know that the majority of the current will be carried near the bottom of the beam. Also, the electric field tends to be concentrated at corners. Due to symmetry, only one half of the beam needs to be modeled. Therefore, the source terms are generated by assuming a unit field strength at the bottom corner, and solving for the field strength at all other nodes with respect to the prescribed node. The current everywhere in the beam is then calculated by dividing the electric field by local resistivity. The current is then normalized with respect to the total rms current found using Eq. (2).

Sample Results for the E-M Model

Figure 4(a) shows a topographical plot of the magnitude of current density in a cross-section of a gold beam 50 µm wide and 2 µm thick. The frequency is 40 MHz, the incident power is 1 W, and the beam temperature is 25°C. By comparison, Fig. 4(b) shows the current density in the same beam with a frequency of 40 GHz. As expected, in both solutions the current is larger in the bottom part of the beam. Moreover, at the higher frequency, the current is much more concentrated along the edges of the beam due to the skin effect. With the current density confined along the edge, the heat generation is expected to be significantly higher at 40 GHz than at 40 MHz due to increased electrical resistance.

Modeling the Temperature Dependence of Current

As long as the beam is isothermal, the current density only needs to be calculated on one cross-section. However, if the temperature varies along the length of the beam, the current density will also vary in this direction due to resistivity changes. While these changes are assumed to be too small to invalidate the 2-D electromagnetic solution, multiple solutions for the cross-sectional current density must be calculated at several points along the beam, as illustrated in Fig. 5. The heat generation between cross-

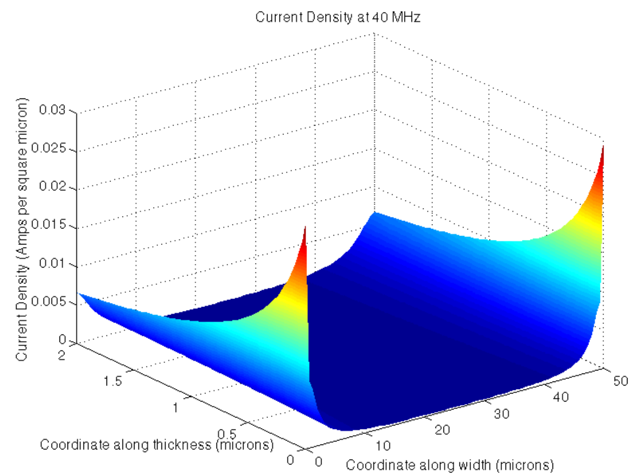

(a)

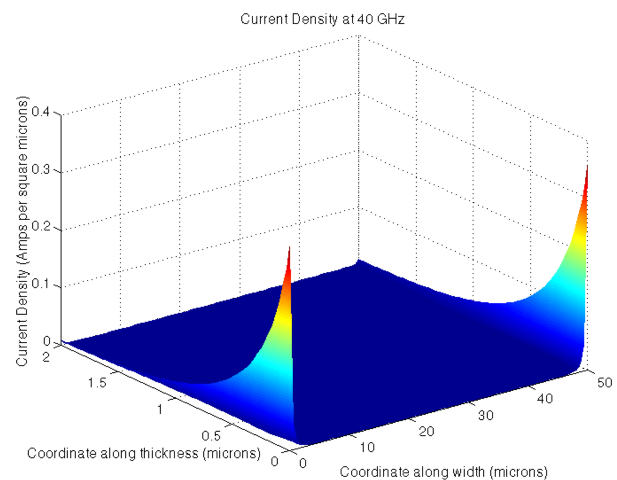

(b)

Figure 4: Current density in a beam 50 mm by 2 mm at 25°C and 1W of transmitted power for (a) 40 MHz and (b) 40 GHz.

sections may then be calculated by assuming linear interpolation of current density along the beam length.

THERMAL MODELING

With the current distribution in the beam calculated, the heat generation at each point may be found using Eq. (1). This heat generation then becomes the input to the thermal model, as indicated by Eq. (3). The temperature distribution was modeled using the finite element method applied to Eq. (3) (for more detail on FEM models of heat transfer, see [19], for example). The Biot number calculated using the beam thickness (0.5-10 µm) lies between 6.3×10^{-8} and 1.3×10^{-6}. Hence, we assume the beam to have nearly constant temperature through its thickness, so that a 2-D FEM simulation may be performed.

The FEM model based on Eq. (3) represents conduction in the beam. For the boundary conditions applied to the model, some estimation of the convective and radiative heat transfer magnitudes is required.

Copyright © 2003 JSME

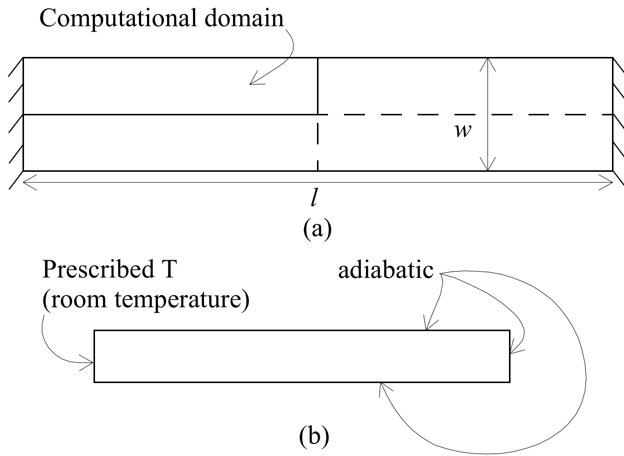

Figure 6: (a) Computational domain and (b) boundary conditions for the heat transfer finite element model.

However, simple calculations indicate that heat transfer due to both convection and radiation is dwarfed by conduction heat transfer. To see this, compare the thermal resistance due to conduction for a point source at the center of the beam

$$R_{cond} = \frac{l}{4\kappa wt} \tag{14}$$

to the convective resistance for an isothermal beam:

$$R_{conv} = \frac{1}{2hlw} \tag{15}$$

In Eq. (15), the factor of 2 represents a very generous estimate for heat transfer from both the top and bottom of the beam. For a gold beam which is 400x50x2 µm, R_{cond} is about 3200 K/W. Assuming a convective heat transfer coefficient of 40 W/m^{2}K, R_{conv} is about 625,000 K/W, or about 200 times as large. Hence, convective heat transfer is expected to be negligible.

Similarly, the heat transfer from the beam due to radiation, assuming the beam is isothermal, is

$$q = \sigma A \varepsilon (T^4 - T_\infty^4) \tag{16}$$

For the same beam, assuming black body radiation and a beam temperature of 670 K (the temperature at which creep may cause failure), the radiative heat transfer is about 0.44 mW, assuming ε is 1 for both the top and bottom of the beam. For the same temperature, the conduction heat transfer calculated using R_{cond} above is about 117 mW. The heat transfer due to conduction is therefore more than 250 times that expected due to radiation. Therefore, in modeling beam temperature, radiative effects can be ignored.

The solution domain and boundary conditions used for solving the beam problem are shown in Fig. 6. Because of symmetry, only one quarter of the beam is discretized and solved. The symmetry ensures adiabatic conditions at the bottom and right of the computational domain, while neglecting convection and radiation results in adiabatic conditions at the top of the domain. At the left, where the beam is fixed to the substrate, the temperature is prescribed as 25°C, or room temperature.

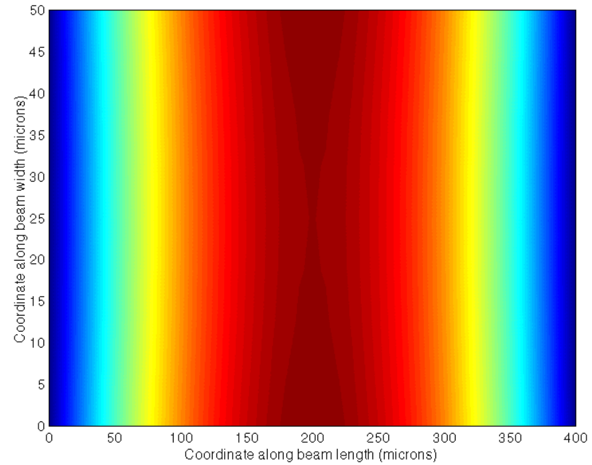

Figure 7: Plot of temperature in the beam with color indicating temperature magnitude.

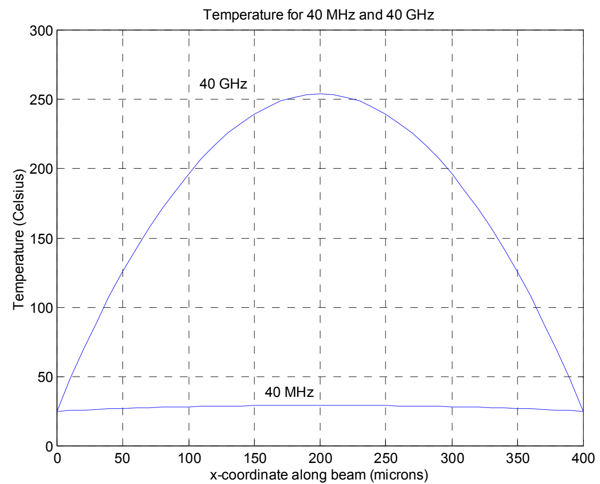

Figure 8: Temperature along the edge of the beam for 40 MHz and 40 GHz

Sample Results for the Combined Model

Execution of the whole algorithm outlined in Fig. 2 allows calculation of beam temperature. Two to three iterations are normally required for convergence to within 1%. Figure 7 shows a plot of the temperature in a gold beam 400x50x2 µm carrying 1 W of power at 40 MHz. The color of the plot represents the temperature. Temperature magnitude along the outside edge of the beam is shown in Fig. 8 for both 40 MHz and 40 GHz. Figure 7 shows that the temperature is slightly higher on the outside edge of the beam than at its center, since most of the current is confined to the outside edge of the beam. However, the steady-state temperature at 40 MHz (29.5°C) is considerably lower than at 40 GHz (~250°C) because of the skin effect. Therefore, the results are consistent with physical expectations. Note that this

Copyright © 2003 JSME

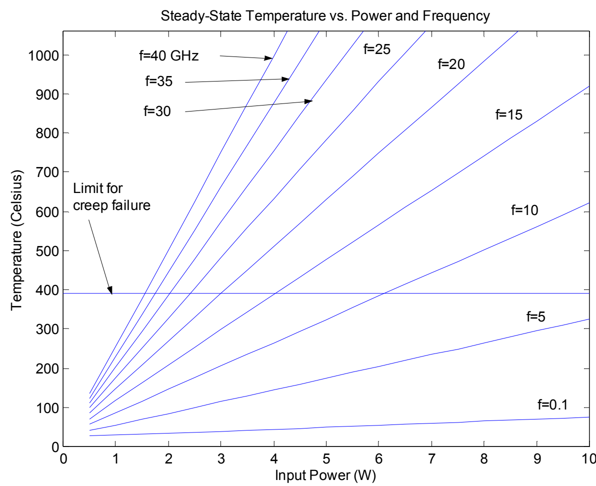

Figure 9: Maximum steady-state temperature in a beam as a function of power and frequency

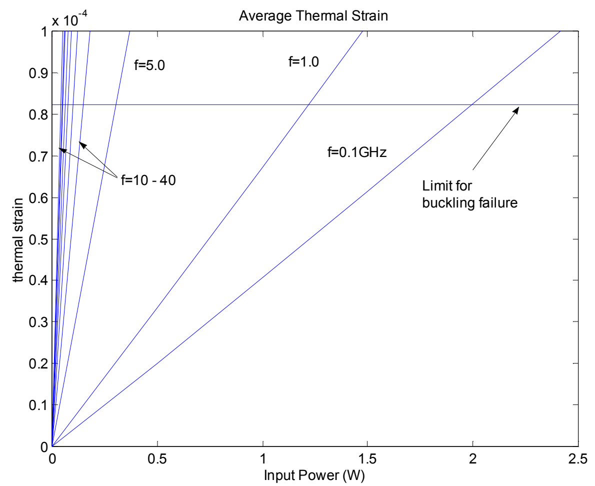

Figure 11: Average thermal strain in the beam as a function of frequency and input power

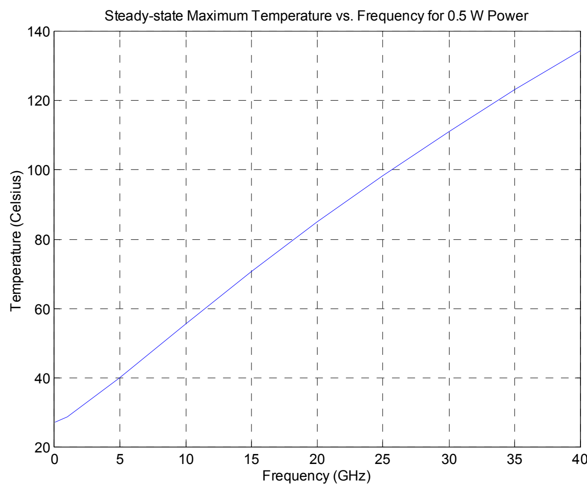

Figure 10: Maximum steady-state temperature as a function of frequency at 0.5 W transmitted power

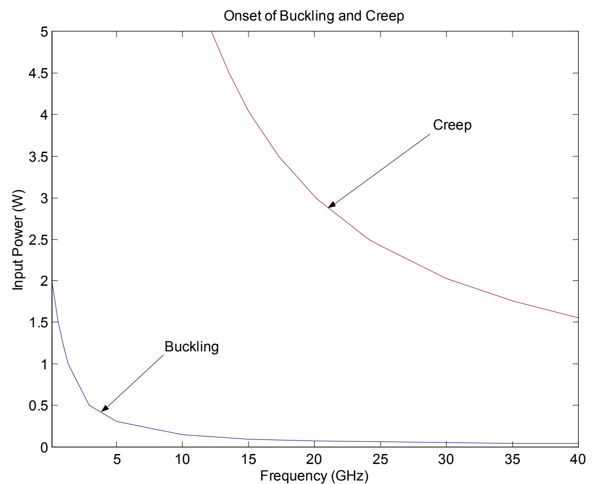

Figure 12: Predicted onset of buckling and creep

represents the first time that the effect of frequency on switch temperature has been modeled.

RESULTS AND DISCUSSION

The maximum steady-state temperature as a function of power and frequency is shown for a gold 400x50x2 μm beam in Fig. 9. The temperature scale has been truncated at 1063°C, the melting point of gold. The limit for expected creep is also marked on the plot. The plot indicates that the temperature varies nearly linearly with power input. Similarly, Fig. 10 shows that temperature also increases nearly linearly with frequency for frequencies above about 2 GHz. This temperature increase, which is due to the skin effect, has not previously been modeled. Below 2 GHz, the skin effect is not as significant.

Using Eq. (6), the average thermal strain in the beam can be found as a function of frequency and power. This strain is plotted for the 400x50x2 μm gold beam in Fig. 11. In this plot, the strain is not shown above 10^{-4}, as buckling occurs above 8.22×10^{-5}, as marked. For most levels of frequency, only a very small power input, below about 0.02-0.05 W, will keep the beam from buckling. Even at very low frequency, where the skin effect is not significant, buckling will occur at about 2.0 W.

The two failure modes studied here, creep and buckling, can be observed together on a contour plot, as shown in Fig. 12. For this geometry, buckling is the dominant failure mechanism for all levels of frequency and power. In fact, buckling is predicted after only 10°C temperature rise for this beam geometry! Moreover, for the first time, buckling and creep are predicted to become more serious as the operating frequency increases. Previous efforts have concentrated almost exclusively on power [9].

CONCLUSIONS AND FUTURE WORK

This paper has modeled the temperature rise in a micromachined RF MEMS switch in the up state due to high-frequency current flow in the beam. First, the current density is calculated using a finite element-boundary

Copyright © 2003 JSME

integral model for a 2-D cross-section of the beam. Heat generation is found by squaring the current density and multiplying by the electrical resistivity. The heat generation is then used in a 2-D finite element model for the temperature in the beam. Because beam temperature affects the material resistivity, the process is iterated using the relaxation technique.

The model was used to calculate temperature rise to allow prediction of the onset of buckling and creep in a gold beam 400x50x2 μm. It was found that for this geometry, creep is not a problem until the transmitted power exceeds more than 1 W even up to 40 GHz. However, buckling is expected to occur for very low power levels (0.02-0.05 W) for most frequencies studied. This is because very small temperature changes can induce buckling of long beams with very small thickness. Therefore, thermal effects are important in determining the failure modes and improving the reliability of RF MEMS switches.

In order to obtain experimental confirmation of the results presented here, testing efforts are underway to measure the temperature rise of several MEMS beams. In addition, the model is being extended to switches in the down state by incorporating electrical and thermal contact resistance modeling. This work will also require extension of the model into the mechanical domain in order to predict the pressure on the contact, an important parameter in contact modeling.

ACKNOWLEDGEMENTS

This work has been supported by the National Science Foundation under Grant No. ECS-0115222. Any opinions, findings, and conclusions or recommendations expressed in this material are those of the authors and do not necessarily reflect the views of the National Science Foundation.

REFERENCES

[1] Yao, J.J., "RF MEMS from a device perspective," *J. Micromech. and Microeng.*, Vol. 10 (2000), pp.R9-R38.

[2] Chang, C. and Peizen, C., "Innovative micromachined microwave switch with very low insertion loss," *Sensors and Actuators A: Physical*, Vol. 79 (2000), pp. 71-75.

[3] Muldavin, J.B. and Rebeiz, G.M., "High-Isolation CPW MEMS Shunt Switches—Part 2: Design," *IEEE Trans. Microwave Theory and Techniques*, Vol. 48, No. 6 (June 2000), pp. 1053-1056.

[4] Park, J.Y., Geun, H.K., Chung, K.W., and Bu, J.U., "Electroplated RF MEMS Capacitive Switches," *Proc. of the IEEE Micro Electro Mechanical Systems (MEMS) 2000*, pp. 639-644.

[5] Muldavin, J.B. and Rebeiz, G.M., "High-Isolation CPW MEMS Shunt Switches—Part 1:Modeling," *IEEE Trans. Microwave Theory and Techniques*, Vol. 48, No. 6 (June 2000), pp. 1045-1052.

[6] Nguyen, C.T.-C., Katehi, L.P.B., and Rebeiz, G.M., "Micromahined Devices for Wireless Communications," *Proc. of the IEEE*, Vol. 86, No. 8 (Aug. 1998), pp. 1756-1768.

[7] Lafontan, X., Dufaza, C., Robert, M., Perez, G., and Pressecq, F., "RF MEMS Micro-Switches Design and Characterization," *Materials and Device Characterization in Micromachining III*, Proc. of SPIE Vol. 4175 (2000), pp. 149-157.

[8] Rebeiz, G.M. and Muldavin, J.B., "RF MEMS Switches and Switch Circuits," *IEEE Microwave Magazine*, Vol. 2, No. 4 (Dec. 2001), pp. 59-71.

[9] Rizk, J.B., Chaiban, E., and Rebeiz, G.M., "Steady State Thermal Analysis and High-Power Reliability Considerations of RF MEMS Capacitive Switches," 2002 IEEE MTT-S Symposium, Seattle, WA.

[10] Senturia, S.D, Aluru, N., and White, J., "Simulating the Behavior of MEMS Devices: Computational Methods and Needs," *IEEE Computational Science and Engineering*, Vol. 4, No. 1 (1997), pp. 30-43.

[11] Aluru, N.R. and White, J., "An efficient numerical technique for electromechanical simulation of complicated microelectromechanical structures," *Sensors and Actuators A: Physical*, Vol. 58 (1997), pp. 1-11.

[12] Funk, J., Korvink, J.G., Bächtold, M., Bühler, J., and Baltes, H., "Coupled 3D Thermo-electro-mechanical Simulations of Microactuators," *Proc. IEEE Micro Electro Mechanical Systems (MEMS) 1996*, pp. 133-138.

[13] Ludwig, R. and Bretchko, P., *RF Circuit Design: Theory and Applications*, Upper Saddle River, New Jersey, Prentice Hall, 2000.

[14] Kittel, C., *Introduction to Solid State Physics*, 6th Ed., New York, John Wiley & Sons, Inc., 1986.

[15] Borden, P.G., "A Novel Method for Measuring the Thermal Conductivity of Electrodeposited Gold Films," *J. Electrochemical Society*, Vol. 127, No. 11 (Nov. 1980), pp. 2454-2457.

[16] Barret, C.R., Nix, W.D., and Tetelman, A.S., *The Principles of Engineering Materials*, Englewood Cliffs, New Jersey, Prentice-Hall, Inc., 1973.

[17] Volakis, J.L., Chatterjee, A., and Kempel, L.C., *Finite Element Method of Electromagnetics*, New York, IEEE Press, 1998.

[18] Jin, J.-J., Volakis, J.L., and Collins, J.D., "A Finite-Element—Boundary-Integral Method for Scattering and Radiation by Two- and Three-Dimensional Structures," *IEEE Antennas and Propagation Magazine*, Vol. 33, No. 3 (June 1991), pp. 22-32.

[19] Hughes, T.J.R., *The Finite Element Method: Linear Static and Dynamic Finite Element Analysis*, Mineola, New York, Dover Publications, Inc., 2000.

Copyright © 2003 JSME